Journal of Quantitative Spectroscopy & Radiative Transfer 178 (2016) 209–223

Contents lists available at ScienceDirect

Journal of Quantitative Spectroscopy & Radiative Transfer

journal homepage: www.elsevier.com/locate/jqsrt

Optical properties of non-spherical desert dust particles in the terrestrial infrared – An asymptotic approximation approach

Lars Klüser [a,*], Claudia Di Biagio [b], Paul D. Kleiber [c], Paola Formenti [b], Vicki H. Grassian [d]

[a] German Aerospace Center (DLR), German Remote Sensing Datacenter (DFD), Oberpfaffenhofen, Wessling, Germany
[b] LISA, UMR CNRS 7583, Université Paris Est Créteil et Université Paris Diderot, Institut Pierre Simon Laplace, Créteil, France
[c] Department of Physics and Astronomy, University of Iowa, Iowa City, IA, USA
[d] Department of Chemistry, University of Iowa, Iowa City, IA, USA

ARTICLE INFO

Article history:
Received 4 September 2015
Received in revised form
24 November 2015
Accepted 24 November 2015
Available online 8 December 2015

Keywords:
Desert dust
Optical properties
Infrared
Non-spherical particles

ABSTRACT

Optical properties (extinction efficiency, single scattering albedo, asymmetry parameter and scattering phase function) of five different desert dust minerals have been calculated with an asymptotic approximation approach (AAA) for non-spherical particles. The AAA method combines Rayleigh-limit approximations with an asymptotic geometric optics solution in a simple and straightforward formulation. The simulated extinction spectra have been compared with classical Lorenz–Mie calculations as well as with laboratory measurements of dust extinction. This comparison has been done for single minerals and with bulk dust samples collected from desert environments. It is shown that the non-spherical asymptotic approximation improves the spectral extinction pattern, including position of the extinction peaks, compared to the Lorenz–Mie calculations for spherical particles. Squared correlation coefficients from the asymptotic approach range from 0.84 to 0.96 for the mineral components whereas the corresponding numbers for Lorenz–Mie simulations range from 0.54 to 0.85. Moreover the blue shift typically found in Lorenz–Mie results is not present in the AAA simulations. The comparison of spectra simulated with the AAA for different shape assumptions suggests that the differences mainly stem from the assumption of the particle shape and not from the formulation of the method itself. It has been shown that the choice of particle shape strongly impacts the quality of the simulations. Additionally, the comparison of simulated extinction spectra with bulk dust measurements indicates that within airborne dust the composition may be inhomogeneous over the range of dust particle sizes, making the calculation of reliable radiative properties of desert dust even more complex.

1. Introduction

Naturally occurring desert dust plays a large role in the climate system (e.g. [1]). Due to strong vibrational resonance bands in the terrestrial infrared (TIR), especially from Si–O and Al–O–H, of clay minerals within the dust plume, desert dust also significantly interacts with TIR radiation. The range of dust particle sizes, typically including particles from sub-micron sizes to several tens of micrometers, further increases the variability of scattering and absorption by desert dust particles. The impact of airborne desert dust on TIR radiation has important implications for climate (e.g. [1,2]) as well as for dust remote sensing at these wavelengths (e.g. [3–5]).

* Corresponding author.
E-mail address: lars.klueser@dlr.de (L. Klüser).

http://dx.doi.org/10.1016/j.jqsrt.2015.11.020
0022-4073/

Desert dust typically consists of a variety of minerals that include quartz, feldspars and several clays (e.g. [6]). A compilation of typical dust compositions has been reported in [5] or in [7]. However, the actual composition of airborne dust can vary significantly in space and time (see for example [6,8,9]). Therefore it is important to reflect these variations in models of TIR scattering and absorption properties.

Many radiative transfer solutions do not necessarily require knowledge of the refractive index, but of the optical (or single scattering) properties themselves, i.e. of extinction efficiency (or coefficient), single scattering albedo and asymmetry parameter or scattering phase function.

As a consequence there is need for reliable TIR optical properties of desert dust for a wide range of applications (see [4,5]). Typically dust optical properties are derived from the complex refractive index using methods relying on spherical (Lorenz–Mie theory) or ellipsoidal respective spheroidal (T-matrix approach) assumptions. Within the Rayleigh limit, that is, for particles having sizes much smaller than the wavelength of incident light, these approaches may become unstable (e.g. [10]).

This current study introduces a fast method to derive the optical properties of (dust) particles with an arbitrary particle size distribution. It is focused on the terrestrial infrared around the resonance bands of dust particles (750–1750 cm^{-1}). The method builds on well-established formulations of scattering and absorption by particles which are either small (Rayleigh limit) or large (geometric optics limit) compared to the wavelength of the incident light. The suitability of the method is evaluated then by comparison with laboratory extinction spectra obtained from Fourier-Transform Infrared (FTIR) spectroscopy as well as with Lorenz–Mie simulations.

The laboratory extinction measurements as well as the compilation of refractive indices for desert dust are explained in Section 2. Section 3 describes the different approaches for calculating optical properties from the spectral refractive index and introduces the asymptotic approximation approach. In Section 4 the results for optical properties of several minerals are presented and analyzed as examples, followed by the comparison of extinction spectra for bulk dust from simulations and measurements in Section 5. The results are discussed in Section 6 while Section 7 summarizes and concludes the paper.

2. Refractive indices and FTIR measurements of desert dust

2.1. Compilation of infrared refractive indices for desert dust components

Desert dust typically consists of external mixtures or aggregates of silicates and a few other minerals. Minerals commonly found in desert dust include quartz, illite, kaolinite, montmorillonite or other smectites as well as feldspars, anhydrite or gypsum and mixtures of calcite and dolomite (e.g. [11,12,5,7]). Moreover also iron oxides contribute to the dust load with high spatial and temporal variability (e.g. [13,6]).

Table 1
Mineral components and corresponding references for the refractive indices used for simulation. All refractive indices used in this study have been obtained by averaging the results from two different sources with equal weights.

Mineral	Sources
Quartz	Spitzer and Kleinman [17], Wenrich and Christensen [18]
Illite	Glotch et al. [19], Querry [20]
Kaolinite	Querry [20], Roush et al. [21]
Montmorillonite	Glotch et al. [19], Querry [20]
Calcite	Lane [22], Long et al. [23]

Refractive indices for the five highly abundant dust minerals quartz, illite, kaolinite, montmorillonite and calcite (e.g. [11,7]) have been compiled from the literature and are tabulated in 1 cm^{-1} increments between 750 and 1750 cm^{-1}. These have been selected due to their significant TIR extinction variability (see e.g. [14–16]). As the literature values from different sources do not always fully coincide with each other, the refractive indices from two different sources for each component have been averaged. Table 1 lists the minerals and the sources for the refractive index data. Quartz and calcite are birefringent minerals. The refractive indices of the ordinary and extraordinary rays have been averaged with a weighting of 2/3 and 1/3, respectively, before performing the simulations. [14] and [15] showed only slight differences in simulations for quartz when the optical constants were averaged spectrally and when the simulations were performed for both rays individually and then averaged. For calcite the differences were higher [14].

2.2. FTIR extinction measurements

FTIR measurements provide an extinction coefficient, that is the extinction due to scattering and absorption by dust particles for a given path length (e.g. [12,14]). Together with dust particle number concentrations and size distributions the extinction coefficient is transferred into extinction efficiency (i.e. extinction cross section divided by geometric cross section). Particle size distribution and number concentration for the measurements used in this study have been determined alongside with the FTIR measurements ([12,14] the effective radii and mass weighted mean diameter are provided in the appendix, Table A.1).

Measurements of extinction spectra for the five single components specified in Table 1 have been performed at the *University of Iowa* and are described in [14]. They are referred to as “Iowa measurements” hereafter.

Extinction spectra of bulk-dust samples have been measured in the 4.2 m^3 CESAM simulation chamber at the *Laboratoire Interuniversitaire des Systèmes Atmosphériques* (LISA) at the *Université Paris Est Créteil* and are referred to as “LISA measurements” in the remainder of this paper. These bulk dust samples have been generated from natural soil samples collected in different areas arid and semi-arid

areas worldwide and have significant contributions of large (supermicron, up to 30 μm in diameter) particles. Full details are provided in [12]. The extinction spectra of these samples are measured after different residence times in the atmospheric simulation chamber. The particle size distribution has been determined together with the extinction measurements (effective radii and mass weighted mean diameter are provided in the appendix, Table A.2) while the composition of the samples has been analyzed a posteriori as well as from the spectra itself [13,12].

3. Simulation of optical properties for spherical and non-spherical particles

3.1. Lorenz–Mie scattering and extinction

Lorenz–Mie solutions for light scattering spheres consist of calculating extinction and scattering efficiencies Q_{ext} and Q_{scat}, respectively, by

$$Q_{ext} = \frac{2}{x^2}\sum_{n-1}^{\infty}(2n+1)\mathrm{Re}(a_n+b_n) \quad (1)$$

$$Q_{scat} = \frac{2}{x^2}\sum_{n-1}^{\infty}(2n+1)\left(|a_n|^2+|b_n|^2\right) \quad (2)$$

The Mie coefficients (a_n and b_n) depend on the complex refractive index as well as on the size parameter $x=2\pi r/\lambda$ and are thus spectral quantities. In this study, the Mie coefficients are calculated with the upward recurrence method [24] using the stability criterions described by [10]. The latter includes breaking the series calculation at $n_{max}=x+4x^{1/3}+2$. Stability conditions and series limits determine the numerical stability of Mie algorithms (e.g. [10,25,24]) and thus the quality of results. The algorithm used for comparison in this study is an adaptation of the Bohren and Huffmann [26] Mie code using upward recurrence. It thus has rather low computational efficiency but likewise high numerical stability.

It is widely known that Lorenz–Mie simulations yield wrong results for non-spherical particles, both in the Rayleigh limit (x«1) and also for larger particles in the Mie scattering size mode (e.g. [5,14,15,16,27]), as it does not account for effects caused by the particle non-sphericity.

3.2. Small particle approximation

For particles in the Rayleigh limit it is often assumed that scattering can widely be neglected and the extinction efficiency is represented by the particle absorption only. For non-spherical particles different approximations of Rayleigh limit absorptions have been formulated ([26]; see also [14,15,16,28]).

Absorption and scattering efficiency in the Rayleigh limit can be described by two approximations for particle shape models which are of special significance for desert dust particles: the “Continuous Distribution of Ellip soids” (CDE) and the “disk” approximations [26,14,15,26]. Following chapter 12 in [26], the corresponding absorption efficiencies are calculated from size parameter x and complex refractive index m as

$$Q_{abs,CDE} = \frac{4}{3}x\mathrm{Im}\left(\frac{2m^2}{m^2-1}\log\left[m^2\right]\right) \quad (3)$$

$$Q_{abs,disk} = \frac{4}{9}x\left(\frac{1}{\left(\mathrm{Re}\left[m^2\right]\right)^2+\left(\mathrm{Im}\left[m^2\right]\right)^2}+2\right)\mathrm{Im}\left[m^2\right] \quad (4)$$

As both are linear in x, the solutions are formally only valid for x«1 (see discussion in [14]).

In these and all equations the radius r in x is assumed to be represented by the radius of a volume equivalent sphere for the respective particle, which allows to use the size parameter x in the calculations.

Corresponding scattering efficiencies for small ellipsoidal particles can be calculated according to chapter 12 in [26]:

$$Q_{sca,CDE} = \frac{8}{27}x^4\left|\frac{2m^2\log(m^2)}{m^2-1}\right|^2 \quad (5)$$

$$Q_{sca,disk} = \frac{8}{81}x^4\left|m^2-1\right|^2\left(\frac{1}{\left(\mathrm{Re}\left[m^2\right]\right)^2+\left(\mathrm{Im}\left[m^2\right]\right)^2}+2\right) \quad (6)$$

Similar Rayleigh-limit solutions for the absorption and scattering efficiencies can also be derived for needle-shaped and spherical particles [26]. As these are only used for comparison of the results for different shapes at one occasion in the paper, the equations are not reproduced here for the sake of readability.

Scattering efficiencies are small in the Rayleigh limit and the scattering phase function is assumed to be represented by the Rayleigh phase function

$$P(\cos\theta) = \frac{3}{4}(1+\cos^2\theta) \quad (7)$$

3.3. Large particle approximation

In the large particle (or geometric optics) limit the Lorenz–Mie solutions for spherical particles show an asymptotic behavior and tend to approximate an analytic solution (e.g. [29,30]). The asymptotic limit for Mie scattering of large spherical particles is

$$Q_{sca,\,\mathrm{lim}} = 1+\left|\frac{m-1}{m+1}\right|^2 \quad (8)$$

When x is in the large particle limit, the curvature radius of the sphere approaches infinity. Thus in the large particle limit all spheres can also be interpreted by Fresnel reflection on flat surfaces (which have curvature radius of infinity). The asymptotic Mie limit presented by [30] suggests $Q_{ext,lim}=2$ regardless of absorption and thus fails to reproduce strong absorption bands where, in fact, the absorption efficiency decreases in spectral ranges of increased $Q_{sca,lim}$. This approximation therefore cannot be used to reliably reproduce the optical properties of airborne particles for example around the strongly absorbing Reststrahlen bands of silicate particles (especially as these particles are not infinitely large). Moreover the asymptotic

limit of Mie particles does not include non-sphericity of the particles.

For reflection at a surface under any incidence angle ϕ the complex angle of refraction is defined by [31,26]

$$\cos(\phi') = \frac{\cos(\phi)}{m} \tag{9}$$

and the Fresnel reflection coefficients are

$$r_1(\phi) = \frac{\sin(\phi) - m\ \sin(\phi')}{\sin(\phi) + m\ \sin(\phi')} \tag{10}$$

$$r_2(\phi) = \frac{m\ \sin(\phi) - \ \sin(\phi')}{m\ \sin(\phi) + \ \sin(\phi')} \tag{11}$$

The Fresnel reflectance at the surface of a large particle (that is, x approaches infinity) follows from Eqs. (10) and (11) as

$$R(\phi) = \frac{1}{2}\left(|r_1(\phi)|^2 + |r_2(\phi)|^2\right) \tag{12}$$

In the large particle limit the scattering efficiency then can be expressed by the angular integral over the Fresnel reflection [31]

$$Q_{sca,Fresnel} = Q_{diff} + \frac{1}{2}\int_0^{\pi/2} R(\phi)\sin\ \phi\ \cos\ \phi\ d\phi \tag{13}$$

where the first summand is the diffraction efficiency (often constantly set to 1) and the second summand (the integral) describes the reflection at the particle surface [26]. In the limiting case of perpendicular incidence the Fresnel reflection approach is equal to the asymptotic Mie solution in the large particle limit.

The Fresnel transmittance can likewise be calculated from

$$t_1(\phi) = \frac{2\ \sin(\phi)}{\sin(\phi) + m\sin(\phi')} \tag{14}$$

$$t_2(\phi) = \frac{2\ \sin(\phi)}{m\sin(\phi) + \ \sin(\phi')} \tag{15}$$

as

$$T(\phi) = \frac{1}{2}\left(|t_1(\phi)|^2 + |t_2(\phi)|^2\right) \tag{16}$$

In contrast to calculating the path of individual rays at the particle surfaces for large particles, the Anomalous Diffraction Theory (ADT) provides an elegant formulation for extinction and absorption efficiencies for optically soft particles [31–33]. We use here the formulation of chapter 11.2 in [31]:

$$Q_{ext,ADT} = 4\ \mathrm{Re}\left(\frac{1}{2} - \frac{\exp(-2xi\cdot(m-1))}{2x\cdot(m-1)} + \frac{\exp(-2xi\cdot(m-1))-1}{(2x\cdot(m-1))^2}\right) \tag{17}$$

$$Q_{abs,ADT} = 1 - 2\frac{\exp(-4xm_i)}{4xm_i} + 2\frac{\exp(-4xm_i)-1}{(4xm_i)^2} \tag{18}$$

The scattering (i.e., in the case of optically soft particles, diffraction) efficiency is not directly determined but results from the difference between extinction and absorption. Strictly speaking, ADT is only valid for particles with $|m-1|\ll 1$ and $x\gg 1$, but the constraint on optical soft particles ($|m-1|\ll 1$) is mainly important for the phase lag of the electromagnetic wave calculated for the extinction efficiency and therefore for the scattered part. [32] nevertheless argue that (for infinitely long cylinders) the errors introduced by deviations from this conditions significantly decrease with increasing absorption, thus they can be assumed to be of minor importance near resonance absorption bands.

As the name already indicates, the anomalous diffraction theory considers the diffraction of the light in optically soft particles and does not reliably take into account the reflection at the particle surface. By combining Eqs. (13), (17) and (19) and substituting the diffraction term in Eq. (13) by the corresponding ADT solution the scattering efficiency for large particles, including diffraction and reflection, can be approximated by

$$Q_{sca,A+F} = \left(Q_{ext,ADT} - Q_{abs,ADT}\right) + \frac{1}{2}\int_0^{\pi/2} R(\phi)\sin\ \phi\ \cos\ \phi\ d\phi \tag{19}$$

The phase function for the large particle approximation directly follows from Eqs. (12), (16) and the angular diffraction pattern [26]. The diffraction contributing to the phase function can be calculated according to [31] as

$$P_{diff}(\theta) = \left(1 - e^{-i\rho\ \sin\ \phi}\right)\cdot J_0(x\theta\ \cos\ \phi)\cdot\ \sin\ \phi\cdot\ \cos\ \phi \tag{20}$$

where J_0 is the zero-order Bessel function, ϕ is the incidence angle as above and the scattering angle θ for the transmitted ray is

$$\theta = 2(\phi - \phi') \tag{21}$$

The combined phase function for the large particle approximation is then simply

$$P_{A+F}(\theta) = P_{diff}(\theta) + R(\phi,\phi') + T(\phi,\phi') + \left(1 - R(\phi,\phi')^2\right)\cdot T(\phi,\phi')^2 \tag{22}$$

where ϕ and ϕ' determine the scattering angle θ. Eq. (22) takes into account the scattered radiation after up to one internal reflection. Higher scattering orders are assumed to be small for strongly absorbing dust particles in the TIR, but can easily be included following the principles of geometric optics.

The scattering efficiency consists of an integral over all incidence angles. Assuming no preferred orientation of the particles and, moreover, facetted rough particle surfaces (e.g. [34]) it seems justified to assume a random distribution of incidence angles.

3.4. Asymptotic approximation approach for non-spherical particles

A simplified solution for extinction and absorption by non-spherical particles can be derived from combining the asymptotic Rayleigh and large particle approximations described above.

A heuristic way to combine the different solutions for small and large particles without strictly separating by a size parameter threshold is to use a weighting function which is nonlinear in x, bound to [0,1] and asymptotically approaches 0 for $x\to 0$ and 1 for $x\to\infty$. This can be

achieved by weighting of the two asymptotic solutions with an exponential decay function in the form

$$\begin{bmatrix} f_1 \\ f_2 \end{bmatrix} = \begin{bmatrix} 1-e^{-y} \\ e^{-y} \end{bmatrix} \tag{23}$$

The sum of f_1 and f_2 always equals 1 and thus this approach does not introduce arbitrary scaling factors to the scattering and absorption solution.

Acknowledging that the validity of the Rayleigh approximation generally requires $x \ll 1$ whereas the validity of the geometric optics solution generally requires $x \gg 1$. None of the solutions is exactly true around $x=1$. For $x>1$ the Rayleigh solution yields inaccurate results, whereas for $x<1$ the large particle approximation also fails to reproduce the optical properties accurately. As a consequence it seems reasonable to separate the regions of applicability for these different approximations at $x=1$, where the weighting fractions are simply postulated to be equal, $f_1=f_2$. While not rigorously correct (as neither solution is rigorously valid at $x=1$), this is a simple heuristic approximation whose validity can be tested experimentally. The equality $f_1(y_0)=f_2(y_0)$ is valid at $y_0=-\ln(0.5)=\ln(2)$. Thus

$$y = -x \cdot \ln\left(\frac{1}{2}\right) = x \cdot \ln(2) \tag{24}$$

in Eq. (23). Strictly speaking, the Rayleigh approaches are valid only *for* $x \ll 1$, while the error of the Fresnel+ADT solution decreases with $x \to \infty$. Consequently both methods are good representations of the asymptotic behavior of extinction spectra in the small and large particle limits, while both may fail to exactly describe the optical properties around $x=1$. Combining both by e^{-x} respective $1-e^{-x}$ yields the asymptotic approximation approach for arbitrary refractive index and particle size:

$$Q_{abs}(m,x) = \left(1-e^{-x\ln(2)}\right) \cdot Q_{abs,ADT}(m,x) + e^{-x\ln(2)} \cdot Q_{abs,Rayleigh}(m,x) \tag{25}$$

$$Q_{sca}(m,x) = \left(1-e^{-x\ln(2)}\right) \cdot Q_{sca,A+F}(m,x) + e^{-x\ln(2)} \cdot Q_{sca,Rayleigh}(m,x) \tag{26}$$

Whether the CDE or the disk (or any other) approximation is used for the Rayleigh approach depends on the mineral component (see [14–16,35]). In order to not include extremely unrealistic spectral features, particle size for the Rayleigh contributions is truncated at $x=1$. That means that for larger particles the scattering and absorption efficiencies of the Rayleigh branch are calculated with the truncation value of $x=1$. Likewise the large particle solution is truncated for $x<1$.

The extinction efficiency and single scattering albedo then are obtained from $Q_{ext}=Q_{sca}+Q_{abs}$ and $\omega_0=Q_{sca}/Q_{ext}$, respectively

The scattering phase function is calculated by

$$P(\theta) = \frac{e^{-x\ln(2)} \cdot Q_{sca,Rayleigh} \cdot P_{Rayleigh}(\theta) + \left(1-e^{-x\ln(2)}\right) \cdot Q_{sca,A+F} \cdot P_{A+F}(\theta)}{Q_{sca,Rayleigh} + Q_{sca,A+F}} \tag{27}$$

and the asymmetry parameter is determined by integration of the scattering phase function over the full scattering domain:

$$g = \int_{-1}^{1} P(\cos(\theta)) \cos(\theta)\, d\cos(\theta) \tag{28}$$

All abovementioned quantities are of course spectral quantities which depend on x and m. In the equations the spectral variables have been omitted everywhere but in Eqs. (27) and (28) for the sake of readability.

4. Comparison of simulated and measured extinction

4.1. Single mineral components

As an example, Fig. 1 shows the extinction and absorption efficiency spectra for quartz and illite as simulated with the lognormal size distributions described in [14] and thus with a non-negligible scattering contribution. The size distribution has been subdivided into 500 radius bins ranging from 0.01 to 40 μm. The blue curves represent CDE simulations, the red curves show Lorenz–Mie results and the black curves indicate the spectra of different fixed shape assumptions in the Rayleigh terms (SDE: “single distribution of ellipsoids”). The solid black line has been determined with the solution for spherical particles, the dashed for disks and the dotted for needle-shaped particles. Comparing the asymptotic approximation for spheres (solid black line) and the Lorenz–Mie solution (red line), the positions of the calculated extinction peaks are similar for both quartz and illite. In addition, for illite the magnitude of the extinction peaks are quite similar while there is some difference in the magnitudes for quartz. This can be seen as evidence that the asymptotic approximation approach can generally yield reliable results (in terms of position and magnitude of the extinction peaks). It also shows that the reliability varies for different minerals, as for example the birefringent mineral quartz shows worse reliability that illite. Moreover the analysis shows the spectral differences between the AAA for non-spherical particles and the Lorenz–Mie simulations are the result of the addition of particle non-sphericity and also of the different methods of calculation.

Fig. 2 shows extinction spectra for quartz, illite, kaolinite and calcite as simulated with AAA (blue) and Lorenz–Mie (red) as well as the corresponding Iowa FTIR measurements (black). The illite spectrum has been simulated with the disk approach in AAA whereas for the other minerals the CDE solution has been used. Fig. 2 also introduces the spectral correlation R^2 (over the full spectral domain) between the simulations and the measurements (color coding refers to the simulation method) as well as the deviation of the peak position D_{pk} from the measurements. It is evident that for the silicates the spectral correlation is much better from AAA than for the Mie simulations and also the shift of the peak position towards higher wavenumbers is turned into a rather weak shift towards lower wavenumbers. Improvements are not evident for calcite. The reason has to be further examined in the future. Using other refractive indices than listed in

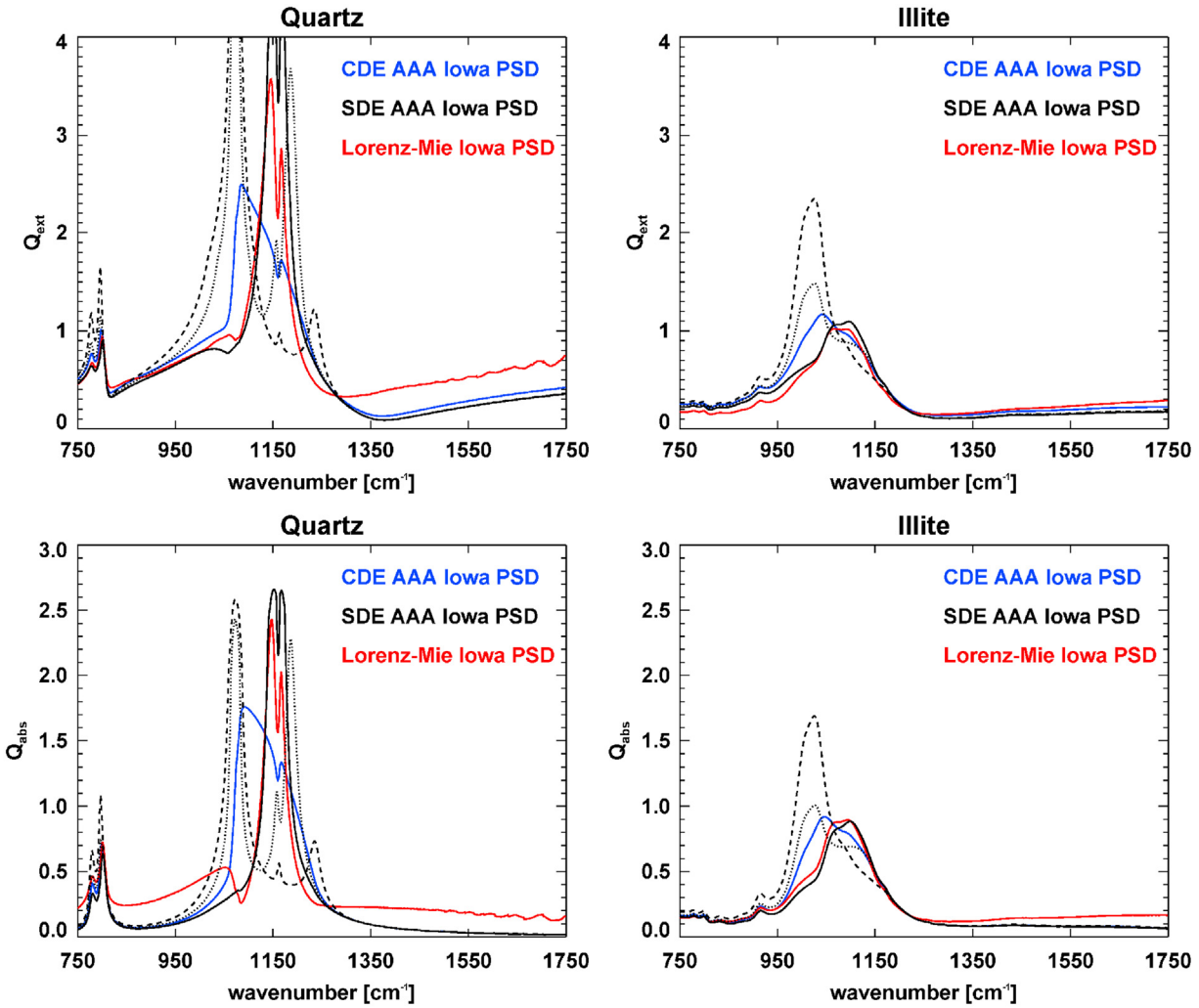

Fig. 1. Extinction (top) and absorption (bottom) efficiencies for quartz (left) and illite (right) calculated with different approaches. The blue curves represent the asymptotic approximation approach with the Rayleigh solutions for continuous distribution of ellipsoids whereas the red curve is the Lorenz–Mie solution. The black curves are derived from the asymptotic approximation approach for singular distributions of ellipsoids where the solid line is for spherical particles, the dashed line for discs and the dotted line for needles. The monomodal lognormal size distributions derived in [14] have been used for all simulations.

Table 1 leads to a further deterioration in the quality of the results (not shown).

Tables 2 and 3 compile the squared correlation coefficient R^2 and the shift of the extinction peak D_{pk} for five different simulation approaches as compared to the Iowa measurements for the five minerals quartz, illite, kaolinite, montmorillonite (spectra not shown as they are rather similar to those of illite) and calcite. It is clearly evident that for quartz the CDE solution is the best approximation to the measurement in terms of correlation and peak position. For the clays the analysis shows that the method with highest correlation does not necessarily also reflect the best approximation to the peak position. For instance the illite correlation is highest with the disk approximation, while the needle approach has an even slightly better correspondence of the peak position. Likewise the correlation is at maximum with CDE for kaolinite and montmorillonite. But for those the peak position is much better approximated with the disk approach (see also [14]). For calcite the Lorenz–Mie simulations result in about the same correlation as the CDE approach but with better localization of the peak maximum. The selection of the Rayleigh method within the AAA simulations has been based on the correlation rather than the peak position for the remainder of this paper. Consequently the disk approximation is used for illite whereas CDE is used for all other minerals (including calcite, where CDE shows the best results of all AAA simulations). Clay minerals typically show a sheeted plate-like structure whereas quartz and calcite take various shapes (see e.g. [36] and also [37]). Consequently these results show a good correspondence with the expectations based on the consideration of real dust particle shapes.

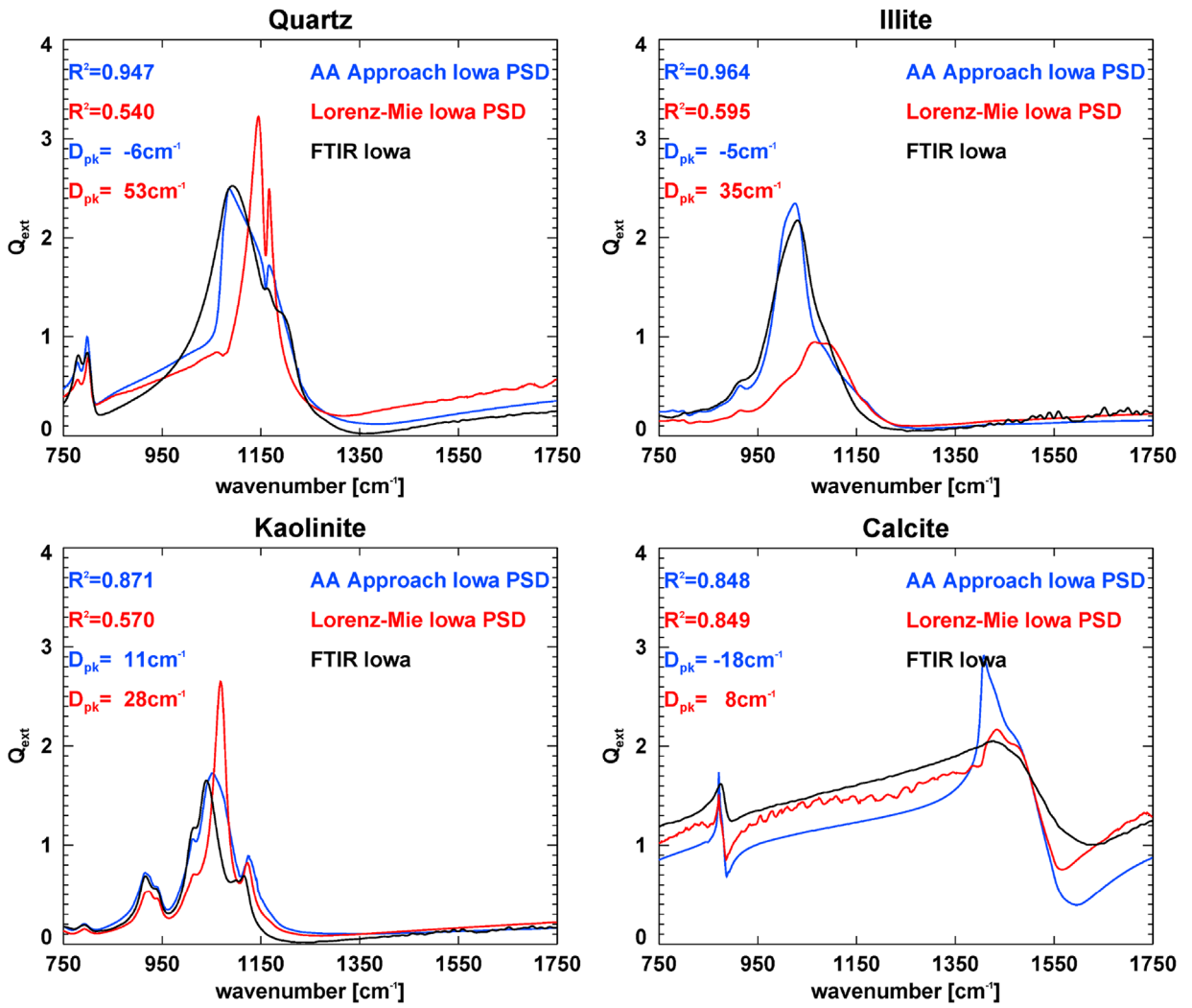

Fig. 2. Extinction efficiencies from Lorenz–Mie solutions (red), the asymptotic approximation approach (blue) and FTIR measurements (black) for quartz (top left), illite (top right), kaolinite (bottom left) and calcite (bottom right). For quartz, kaolinite and calcite the CDE shape model is used in the AAA, for illite the disk model. Size distributions and FTIR measurements are from [14]. Squared correlation coefficients (R^2) and the deviations of the peak position (D_{pk}) are presented for the simulations in the respective color coding.

Table 2
Squared correlation coefficient between FTIR extinction efficiency spectra and simulated ones for the different Rayleigh approximations and the five minerals.

R^2	*Quartz*	*Illite*	*Kaolinite*	*Montmorillonite*	*Calcite*
CDE	0.947	0.851	0.871	0.823	0.848
Disk	0.737	0.964	0.833	0.811	0.761
Needle	0.728	0.925	0.753	0.789	0.741
Sphere	0.457	0.595	0.445	0.578	0.741
Lorenz–Mie	0.540	0.595	0.570	0.800	0.849

Fig. 3 presents simulations of single scattering albedo and asymmetry parameter spectra for quartz and for illite (results from the same simulations as described above: CDE shape model used for quartz and disk shape model for illite). The magnitude of the single scattering albedo is comparable for AAA and Lorenz–Mie in wide parts of the spectral domain for illite. For quartz partly strong differences of the single scattering albedo can be observed.

The spectral evolution of the asymmetry parameter is rather similar for the AAA solution and the Lorenz–Mie simulations. At most positions the AAA asymmetry parameter is slightly lower than that from Mie theory. A significant difference between AAA and Lorenz–Mie results is found around 1350 cm^{-1} for quartz. The reason is that in the disk solution for small particles (like used for illite) the scattering efficiency approaches zero at the Christiansen wavelength [38] where $|m^2-1|$ approaches zero. The same drop of Q_{sca} is found in the large particle approximation. In the CDE Rayleigh approach this drop of Q_{sca} is not present. As the phase functions of the small and large particle approximations are weighted by the corresponding scattering efficiency, $Q_{sca,CDE}$ gets relatively more weight than

Table 3
Shift of the extinction peak position in the simulated extinction efficiencies compared to FTIR spectra for the different Rayleigh approximations and the five minerals.

D_{pk}	*Quartz* (cm^{-1})	*Illite* (cm^{-1})	*Kaolinite* (cm^{-1})	*Montmorillonite* (cm^{-1})	*Calcite* (cm^{-1})
CDE	−6	+12	+11	+18	−18
Disk	−10	−5	−7	+0	−23
Needle	−10	−4	+45	+2	−23
Sphere	+49	+65	+32	+33	+55
Lorenz–Mie	+53	+35	+28	+30	+8

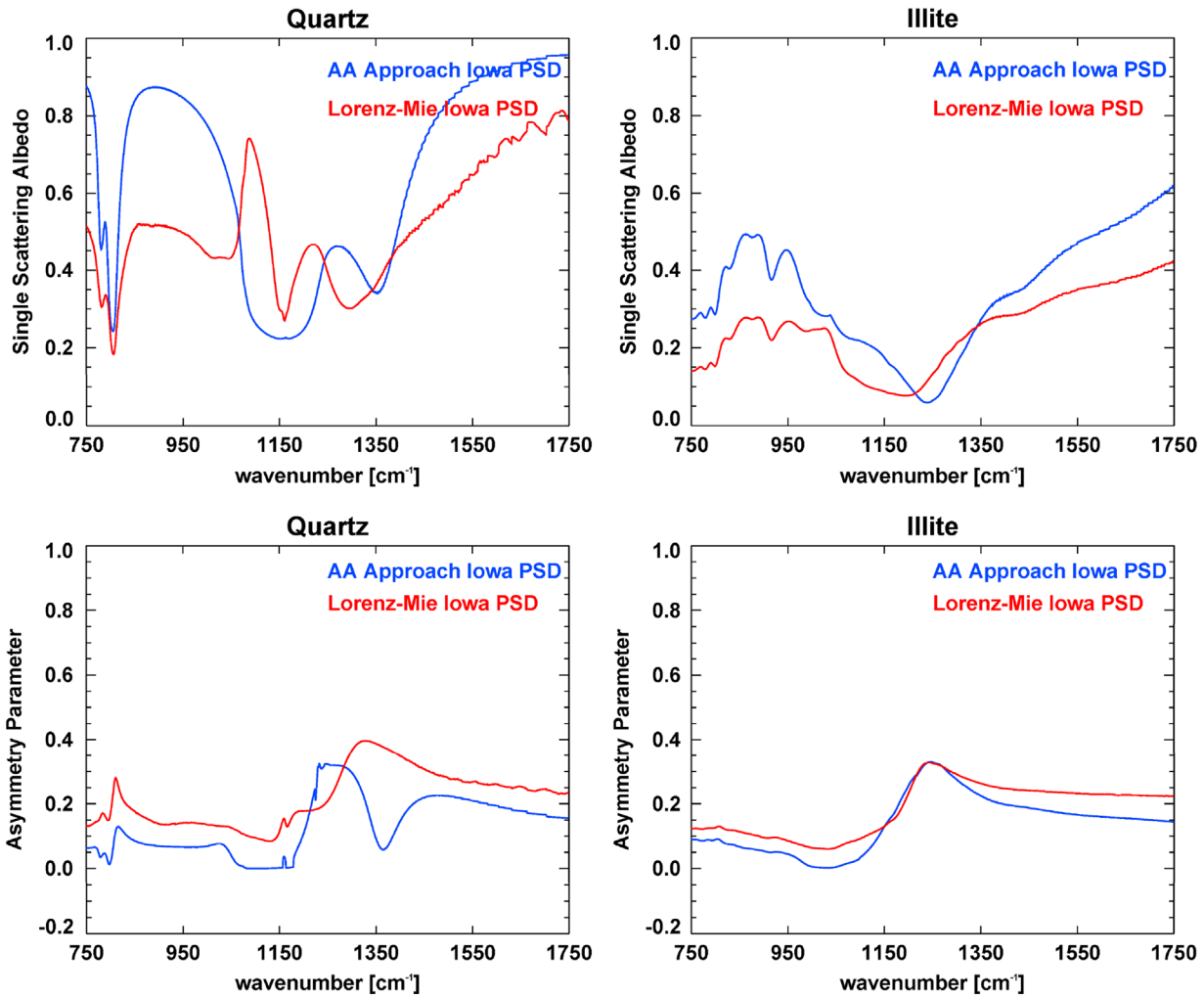

Fig. 3. Single scattering albedo (top) and asymmetry parameter (bottom) for quartz (left) and illite (right) in the monomodal lognormal particle size distribution from [14]. The blue curves represent the asymptotic approximation approach and the red curves originate from the Lorenz–Mie solutions.

$Q_{sca,A+F}$ and consequently the Rayleigh phase (with $g=0$) function outweighs the geometric optics phase function.

Fig. 4 depicts the scattering phase functions for quartz and illite. The spectral evolution is shown for the AAA solutions for both minerals together with the phase functions at 950 and 1700 cm^{-1}. It can be seen that for both minerals the phase functions at 950 cm^{-1} look rather similar for the AAA and Lorenz–Mie solutions whereas at higher wavenumbers the AAA solution tends to reproduce a significant forward peak which is not as evident from the Lorenz–Mie simulations. It seems to be due to the shifted position of the minimum of the scattering phase function that the asymmetry parameter from the Lorenz–Mie solutions nevertheless is slightly larger than that of the AAA simulations. As the scattering phase function in this spectral region has not been measured in the laboratory it cannot be analyzed if the AAA improves results in comparison with the Lorenz–Mie theory, which assumes

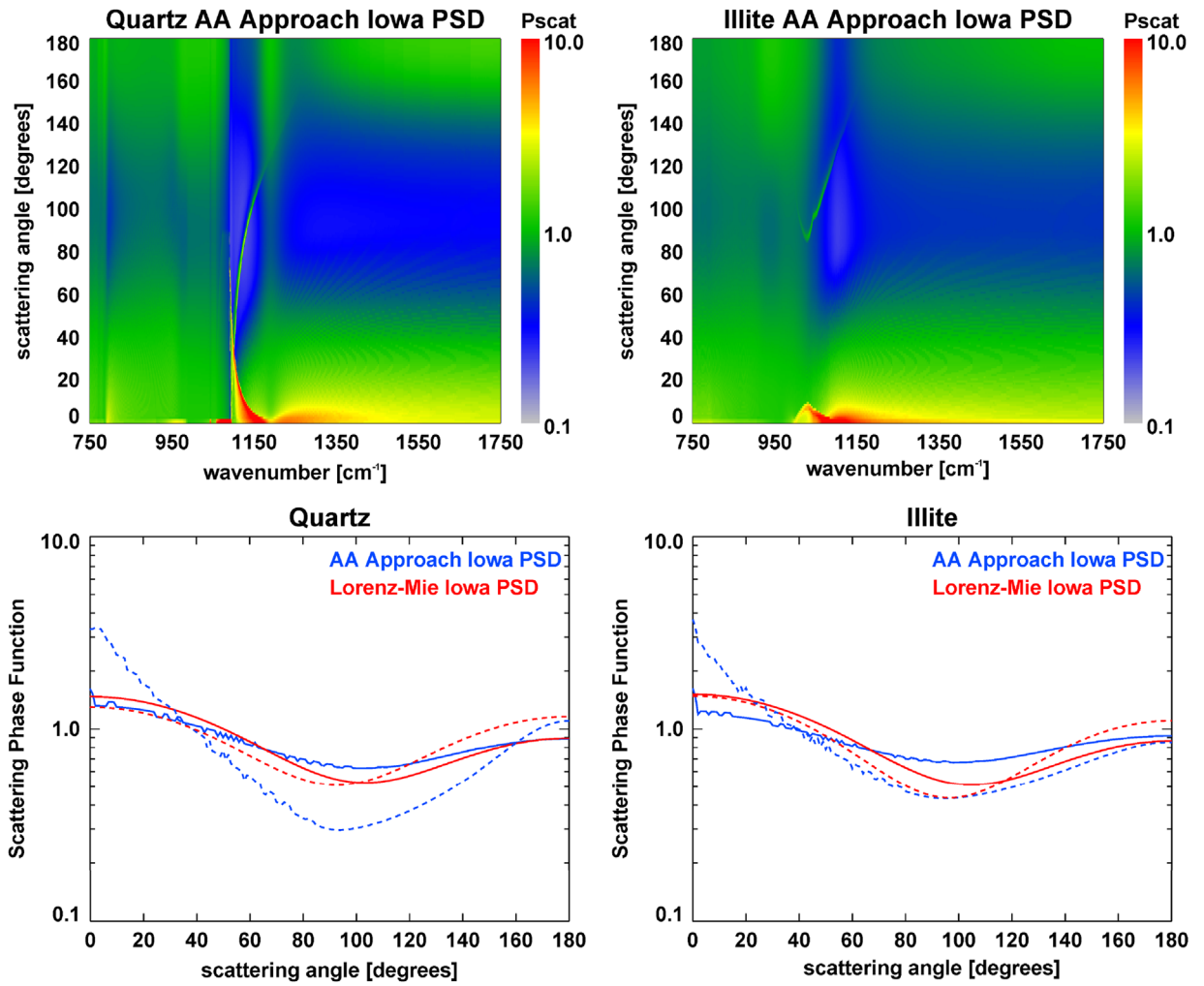

Fig. 4. Scattering phase function for for quartz (left) and illite (right) in the monomodal lognormal particle size distribution from [14]. The upper panel shows the spectral phase function of the asymptotic approximation approach whereas the lower panel depicts phase functions of the AAA (blue) and Lorenz–Mie (red) simulations evaluated at 950 cm^{-1} (solid) and 1700 cm^{-1} (dashed).

spherical particles, or if the derived asymmetry parameter is correct.

4.2. Natural dust samples

Fig. 5 shows extinction spectra of bulk dust samples from Nigeria and from China with two different size distributions resulting from residence time in the atmospheric simulation chamber (see [12] for details). Besides the LISA measurements also simulations of these spectra with the AAA method and with Lorenz–Mie theory are presented. The simulations have been performed with effective refractive indices calculated iteratively using the Maxwell-Garnett effective medium approach [39] from the refractive indices of the different dust components weighted according to their abundance. The mineralogical composition of the two dust samples is derived from [13]. The relative contributions of the five minerals used in this study for the simulation is reproduced in the appendix (Table A.2).

The “Niger1” and “China1” spectra are those measured at the early stage of the experiment, so with the largest fraction of supermicron particles, while “Niger3” and “China3” represent the extinction spectra after 50-minute residence time, when a part of the supermicron fraction has deposited by gravitational settling [12]. The AAA solution has been calculated with the CDE approach for the Rayleigh limit. As before (for the silicates) the correlation with the measurement is higher for the AAA solution than for the Lorenz–Mie solution. The spectral correlations decrease after the residence time in the atmospheric chamber for the China sample, but the inverse is observed for the Niger sample. Peak shifts have not been calculated for the bulk dust spectra, as several local peaks of the different abundant minerals contribute to the overall spectrum. Nevertheless it can be seen from the spectra that the position of the major (silicate) extinction peaks are well reproduced by the simulations with both methods. The extinction at high wavenumbers (1300–

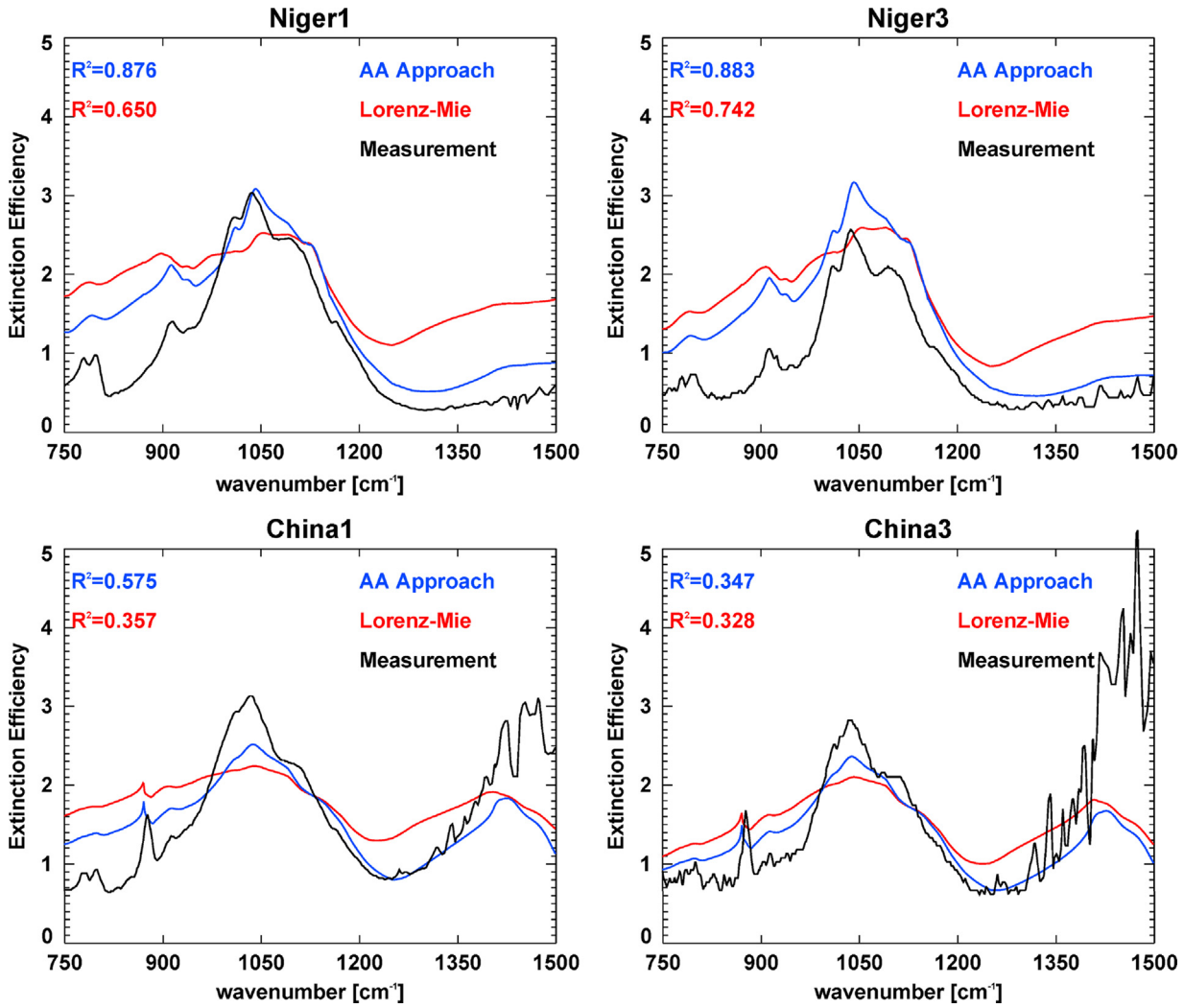

Fig. 5. Extinction efficiency from bulk dust laboratory measurements (black) as well as Lorenz–Mie (red) and asymptotic approximation approach (blue) solutions for particles directly after injection (left) and after 50 minutes residence time (right) for dust samples from Niger (top) and China (bottom). Effective medium refractive indices combining the refractive indices of the different dust components with the Maxwell-Garnett approached have been used for the simulations.

1500 cm^{-1}) due to calcite abundance in the China sample is reproduced by the simulations qualitatively but not quantitatively.

Fig. 6 shows a similar analysis as Fig. 5. The only difference is that for these simulations the extinction spectra for the different mineralogical components abundant in the samples have been calculated and afterwards averaged according to their relative abundance (this approach has also been used in [5]). In contrast to the above results for the China spectra, the correlations of the Lorenz–Mie simulations with the measurements are slightly higher (while still weak) than those of the AAA calculations. For the Niger samples the AAA solution again correlates better with the FTIR spectra than the Lorenz–Mie method. The Lorenz–Mie simulations for both samples fail to correctly reproduce the position of the main extinction peaks, showing a significant shift towards higher wavenumbers in the Lorenz–Mie results.

It can be observed that the largest deviations between AAA spectra (and also Lorenz–Mie solutions) and measurements for the China sample occur at wavenumbers well above 1200 cm^{-1}. Fig. 2 suggests that the extinction at these wavenumbers is dominated by calcite, which moreover shows the worst correlation of all single mineral comparisons as well as a rather weak reproduction of the extinction peak position. Moreover, calcite is the only mineral where the Lorenz–Mie simulations show better correspondence to the Iowa measurements than the AAA simulations.

If only the spectral range between 800 and 1250 cm^{-1} is considered, the AAA simulations well represent the measurements whereas the Lorenz–Mie simulations show the typical shift of the extinction peaks towards higher

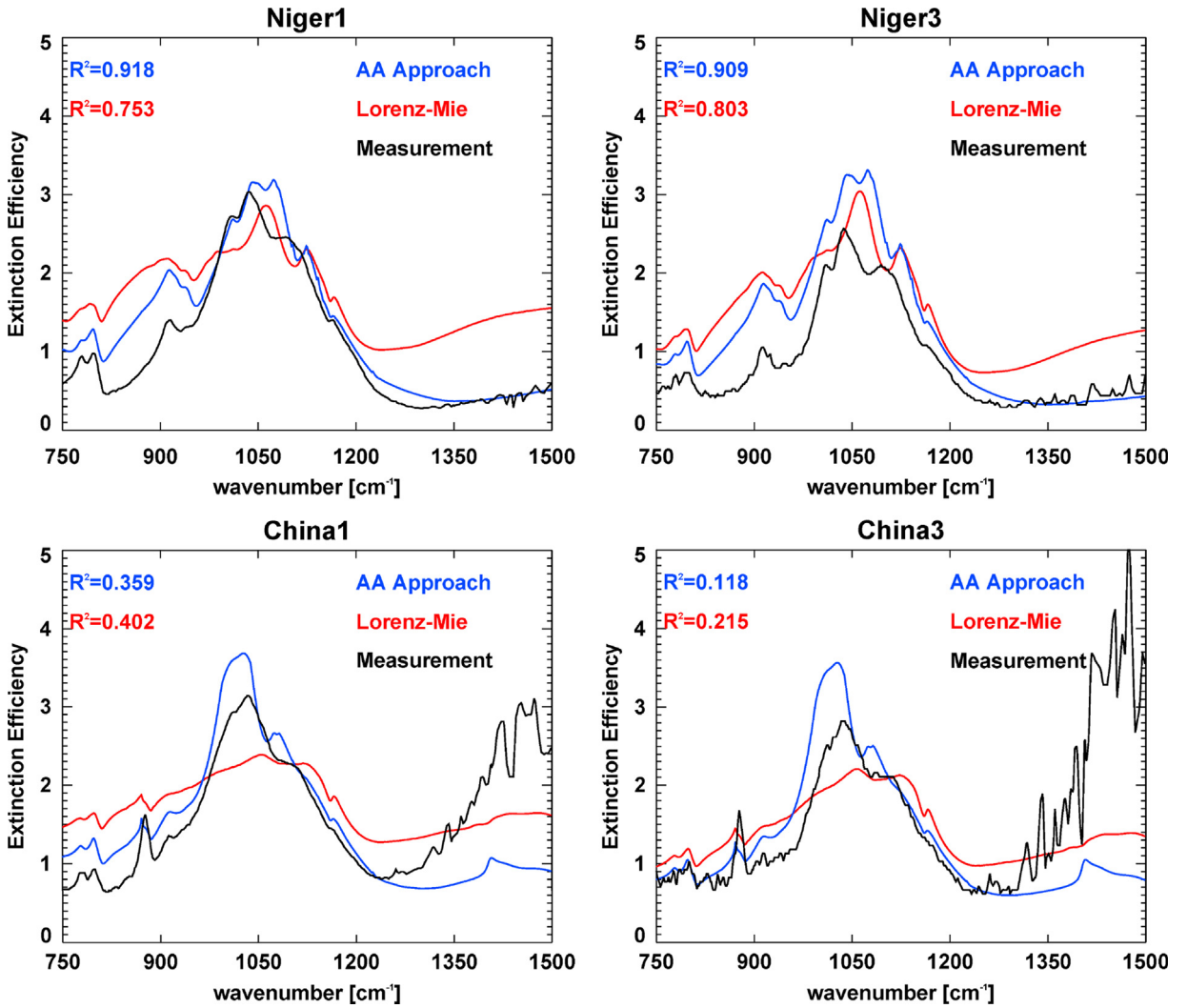

Fig. 6. Extinction efficiency from bulk dust laboratory measurements (black) as well as Lorenz–Mie (red) and asymptotic approximation approach (blue) solutions for particles directly after injection (left) and after some residence time (right) for dust samples from Niger (top) and China (bottom). All simulated spectra are based on averaging of the corresponding optical properties of individual minerals contributing to the dust mixture.

wavenumbers (Fig. 7). The calcite extinction peak at higher wavenumbers does not have a large effect on the spectrum in this domain and consequently the correlations of both methods for the China sample increase significantly. This spectral domain is the most important one for dust remote sensing in the TIR whereas the spectral domain of the strong calcite peak is dominated by water vapor absorption in the atmosphere and thus cannot be used for dust remote sensing (e.g. [5]). The simulations using effective medium refractive indices calculated with the Maxwell-Garnett approach (see full-domain spectra in Fig. 5) yield correlations over the window region spectral range which do not significantly deviate from those presented in Fig. 7 (not shown). Consequently both, effective refractive indices as well as averaged optical properties can be used for simulating the single scattering properties of desert dust mixtures in the TIR window.

5. Discussion

The asymptotic approximation approach for calculating the single scattering properties of non-spherical dust particles is able to well reproduce the spectral variation of extinction by silicate dust components. Compared with Lorenz–Mie simulations it shows an improvement in spectral correlation and peak position with respect to laboratory measurements. The results for calcite are not as convincing. In fact, for the pure calcite spectrum the spectral correlation is (very slightly) higher for the Lorenz–Mie calculations than for the AAA method.

These problems in reproducing the calcite peak between 1400 and 1700 cm^{-1} directly impact on the correspondence between simulations and measurements for bulk dust samples. Both methods (Lorenz–Mie and AAA) widely fail to reproduce this calcite peak in the LISA measurements. The low correspondence especially for the

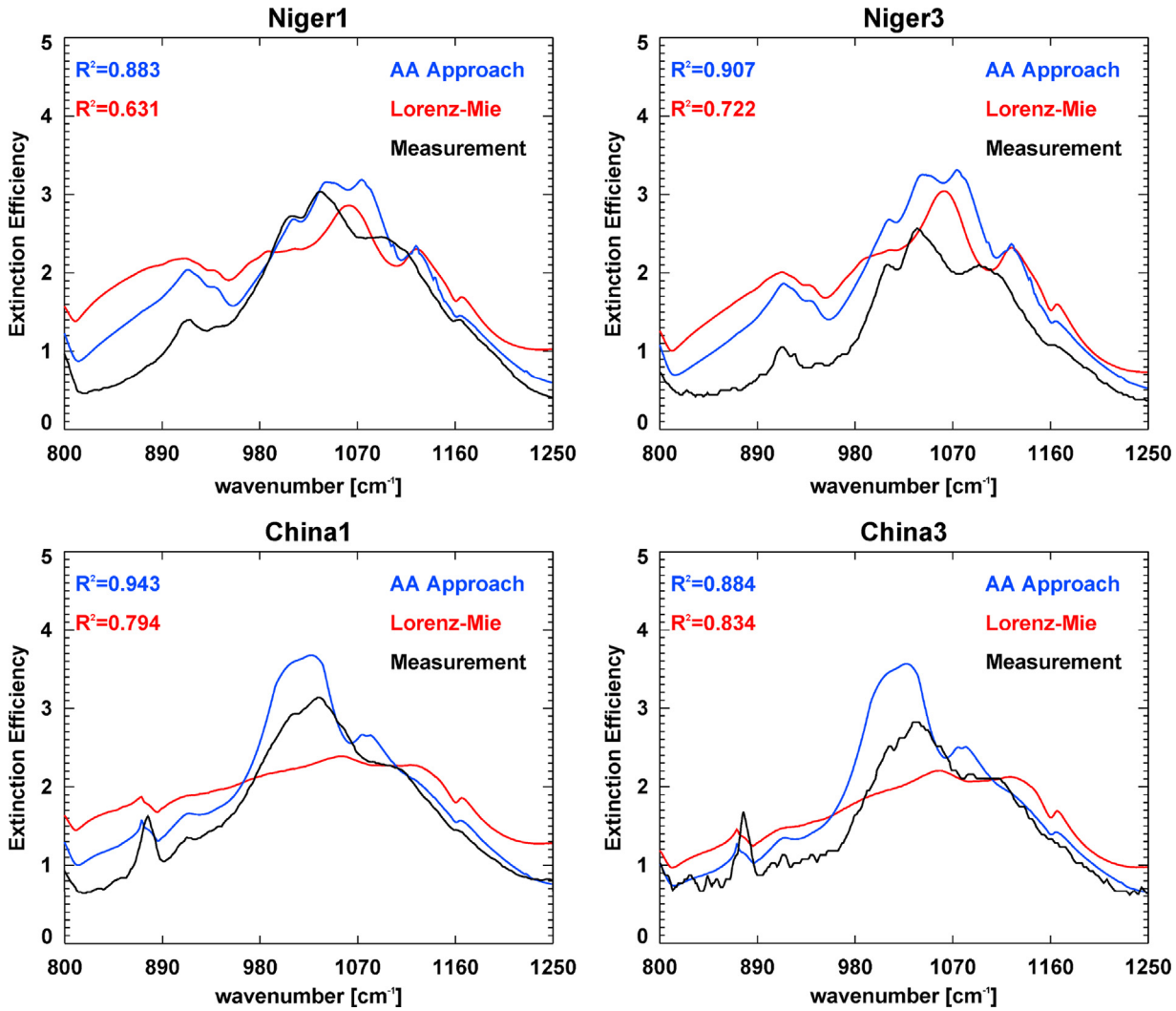

Fig. 7. Window region only extinction efficiency from bulk dust laboratory measurements (black) as well as Lorenz–Mie (red) and asymptotic approximation approach (blue) solutions for particles directly after injection (left) and after some residence time (right) for dust samples from Niger (top) and China (bottom). All simulated spectra are based on averaging of the corresponding optical properties of individual minerals contributing to the dust mixture.

calcite peak points towards two important lessons. One is that the optical properties of calcite still seem to require some more attention, as for calcite generally significant problems in reproducing the extinction spectrum occur (potentially due to an incorrect modeling of the scattering at higher wavenumbers). Especially for calcite there is a large impact of particle size on the relative significance of the different absorption peaks and on the spectral shape of the extinction signal (see comparison in [14]). In all simulations performed in this study the mineralogical composition of the dust is assumed to be independent of the size distribution. This has been shown to be not always true (e.g. [13,40]). Moreover it is assumed that the abundant minerals are distributed equally over the size ranges of the dust size distribution. The results observed here seem to indicate that these two assumptions might be an oversimplification and that mineral composition could as well be varying with particle size.

All results of optical properties shown and examined here are those for pure dust suspended in an otherwise transparent medium (clean air). Also the extinction efficiency is not affected by thermal emission from the dust itself. In any application, be it remote sensing or climate studies, the problem is much more complex due to the effect of masking by absorbing gases, by effects of the thermal contrast between the dust layer and the underlying surface (e.g. [3]) as well as imperfect knowledge about dust composition and chemical mixture with other aerosols such as sea salt or industrial sulfates. Thus a lot of the spectral differences found here for different dust compositions might not be as significant in atmospheric spectra as in the laboratory measurements. Nevertheless it has been shown previously, that space-

borne measurements from hyperspectral infrared sounders such as the Infrared Atmospheric Sounding Interferometer (IASI) can be used to discriminate signals of dust composition from space [41,5].

Whether it is better to use effective refractive indices or to simulate the optical properties of single minerals and then average according to their abundance is not entirely clear from the comparisons with the LISA measurements for bulk dust presented above. The Niger sample would suggest that averaging the optical properties is more reliable whereas for the China sample it seems to be vice versa. The latter conclusion mainly stems from the better representation of the calcite extinction peak at high wavenumbers in the effective medium approach. For the atmospheric window region the correlations are quite similar between effective refractive indices and averaged optical properties.

While the correspondence between simulations and measurements is rather weak for the calcite-bearing bulk dust sample, the results significantly improve for the 800 to 1250 cm^{-1} atmospheric window region. For atmospheric remote sensing the calcite extinction at higher wavenumbers is masked by strong water vapor absorption bands in this region. Consequently the imperfect simulation of the calcite extinction here has only minor impacts on the usability of the simulations for remote sensing (and climate) applications.

The reliability of the asymptotic approximation approach has been analyzed in terms of the spectral shape of extinction spectra as well as the position of the major extinction peaks. Although also single scattering albedo and asymmetry parameter as well the scattering phase functions have been shown, the comparison with Lorenz–Mie simulations shows discrepancies between both approaches. The FTIR measurements performed at the University of Iowa and at the LISA laboratory cannot be used to judge which one better represents the full single scattering properties of desert dust. Consequently in a subsequent study the asymptotical approximation approach will be compared with simulations by more exact methods for non-spherical dust particles, such as T-matrix simulations (e.g. [42]). Only then can the accuracy of the method can be fully evaluated. This work is focused on introducing and testing the method as a means for simulating the spectral shape of the IR extinction profiles through a quantitative comparison to results from laboratory measurements. It is beyond the scope of this paper to fully address the accuracy of single scattering albedo and phase function. This topic will be covered in a dedicated study in the future.

6. Conclusions

A simple method for simulating single scattering properties of dust particles in the terrestrial infrared based on asymptotic approximations for scattering and absorption in the Rayleigh-mode as well as on anomalous diffraction theory and large particle limits for scattering and absorption has been presented. Extinction simulations with this method have been compared to independent measurements of both, single component dust and bulk dust collected in desert environments as well as to simulations with Lorenz–Mie theory. The asymptotic approximation approach improves the results insofar that the spectral extinction patterns of single minerals better coincide with the measurements than for the Lorenz–Mie simulations.

It has also been shown that for bulk dust reliable spectra can be simulated with the AAA method as well. Spectral correlation reaches values as high as $R^2=0.92$ over the full spectral domain and $R^2=0.94$ in the atmospheric window.

The comparison with extinction measurements of bulk dust from desert environments at different times after injection into the measurement chamber showed that the calcite extinction in the China sample is not well reproduced in the simulated optical properties. In current applications such as remote sensing and climate studies (including dust modeling) size-dependent dust composition is not yet considered. Nevertheless the results presented here suggest that in some cases the radiative properties may highly depend on the proper characterization of dust composition in different size classes. Subsequent work will address the characterization of the dust composition in different particle size classes or modes of the particle size distribution.

The asymptotic approximation approach is much faster than Mie calculations, as no iterative Bessel functions have to be calculated and as it is not subject to (theoretically infinite) series expansion. Moreover it is suitable for different particle shapes, also such deviating from any spheroidal assumption. For example it is as well possible with this approach to calculate optical properties of cylindrical or cubic particles over a wide range of particle sizes. Also preferred particle orientation can easily be included in the simulations.

AAA single scattering albedo and asymmetry parameter show approximately the same magnitude as from Lorenz–Mie simulations. Nevertheless the also show spectral discrepancies, which cannot be explained only by the shift in the positions of absorption peaks. As these quantities have not been measured in the laboratory, it is so far impossible to assess if the asymptotic approximation approach yields reliable results with respect to the scattering phase function and single scattering albedo. A subsequent study will investigate these quantities by comparison with the T-matrix method.

Acknowledgments

L. Klüser's contribution to this research was supported by the European Space Agency (ESA) as part of the Aerosol_cci project (ESA Contract no. 4000109874/14/I-NB). C. Di Biagio was supported by the Centre National des Etudes Spatiales (CNES) and by the CNRS via the Labex L-IPSL. The

CESAM chamber was supported by the European Commission (EC) within the I3 project "Integration of European Simulation Chambers for Investigating Atmospheric processes" (EUROCHAMP-2, contract 228335) and by OSU-EFFLUVE (Observatoire des Sciences de l'Univers-Enveloppes Fluides de la Ville à l'Exobiologie) through dedicated research funding. P. Kleiber and V. Grassian acknowledge that this material is in part based upon work supported by the US National Science Foundation under Grant no. ATC-1439045. Any opinions, findings, and conclusions or recommendations expressed in this material are those of the authors and do not necessarily reflect the views of the National Science Foundation.

We also thank two anonymous reviewers for their constructive comments.

Appendix A

Effective radius and mass weighted mean diameter are defined as.

$$R_{eff} = \frac{\int R^3 n(R)\, dR}{\int R^2 n(R)\, dR} \tag{A.1}$$

$$D_w = \frac{\int D^4 n(D)\, dD}{\int D^3 n(D)\, dD} \tag{A.2}$$

See Tables A.1 and A.2.

Table A.1
Effective radii (R_{eff}) and mass-weighted mean diameter (D_w) for the size distributions of the samples used in this study. The D_w values of quartz and calcite presented here deviate from those calculated [14] because of a truncation of the size distribution at maximum particle radius of 40 μm.

Sample	R_{eff} (μm)	D_w (μm)	Sample	R_{eff} (μm)	D_w (μm)
Iowa Quartz	1.09	10.46	LISA Niger1	3.22	8.46
Iowa Illite	0.50	2.42	*LISA Niger3*	2.30	5.98
Iowa Kaol.	0.61	3.11	*LISA China1*	2.76	7.63
Iowa Calcite	2.97	16.44	*LISA China3*	1.90	5.58

Table A.2
Estimated composition for the simulations for LISA dust samples (see [13,12]). The numbers have been obtained by averaging the fine and coarse modes from [13] Table 2 and normalization to the five minerals taken into account here. The clay mineral partitioning has been performed by using illite/kaolinite ratios of 0.1 for Niger and 5.0 for China [43,44].

Mineral	**Niger (%)**	**China (%)**
Quartz	27.2	21.6
Illite	6.9	42.7
Kaolinite	64.4	8.5
Calcite	1.5	27.2

References

[1] Shao Y, Klose M, Wyrwoll K-H. Recent global dust trend and connections to climate forcing. J Geophys Res Atmos 2013;118:11,107–18. http://dx.doi.org/10.1002/jgrd.50836.
[2] Huang J, Wang T, Wang W, Li Z, Yan H. Climate effects of dust aerosols over East Asian arid and semiarid regions. J Geophys Res Atmos 2014;119:11,398–416. http://dx.doi.org/10.1002/2014JD021796.
[3] Ackerman SA. Remote sensing aerosols using satellite infrared observations. J Geophys Res 1997;102:17069–79.
[4] Banks JR, Brindley HE, Flamant C, Garay MJ, Hsu NC, Kalashnikova OV, Klüser L, Sayer AM. Intercomparison of satellite dust retrieval products over the west African Sahara during the Fennec campaign in June 2011. Remote Sens Environ 2013;136:99–116.
[5] Klüser L, Banks JR, Martynenko D, Bergemann C, Brindley HE, Holzer-Popp T. Information content of space-borne hyperspectral infrared observations with respect to mineral dust properties. Remote Sens Environ 2015;156:294–309. http://dx.doi.org/10.1016/j.rse.2014.09.036.
[6] Formenti P, Caquineau S, Chevaillier S, Klaver A, Desboeufs K, Rajot JL, Belin S, Briois V. Dominance of goethite over hematite in iron oxides of mineral dust from Western Africa: quantitative partitioning by X-ray absorption spectroscopy. J Geophys Res 2014;119:12,740–54. http://dx.doi.org/10.1029/2014JD021668.
[7] Scanza RA, Mahowald N, Ghan S, Zender CS, Kok JF, Liu X, Zhang Y, Albani S. Modeling dust as component minerals in the community atmosphere model: development of framework and impact on radiative forcing. Atmos Chem Phys 2015;15:537–61. http://dx.doi.org/10.5194/acp-15-537-2015.
[8] Glaccum RA, Prospero JM. Saharan aerosols over the tropical North Atlantic – Mineralogy. Mar Geol 1980;37:295–321.
[9] Usher CR, Michel AE, Grassian VH. Reactions on mineral dust. Chem Rev 2003;103:4883–939.
[10] Wiscombe WJ. Improved Mie scattering algorithms. Appl Opt 1980;19(9):1505–9.
[11] Sokolik IN, Toon OB. Incorporation of mineralogical composition into models of the radiative properties of mineral aerosol from UV to IR wavelengths. J Geophys Res 1999;104(D8):9423–44.
[12] Di Biagio C, Formenti P, Styler SA, Pangui E, Doussin J-F. Laboratory chamber measurements of the longwave extinction spectra and complex refractive indices of African and Asian mineral dusts. Geophys Res Lett 2014;41(17):6289–97. http://dx.doi.org/10.1002/2014GL060213.
[13] Lafon S, Sokolik IN, Rajot JL, Caquineau S, Gaudichet A. Characterization of iron oxides in mineral dust aerosols: Implications for light absorption. J Geophys Res 2006;111:D21207. http://dx.doi.org/10.1029/2005JD007016.
[14] Mogili PK, Yang KH, Young MA, Kleiber PD, Grassian VH. Extinction spectra of mineral dust aerosol components in an environmental aerosol chamber: IR resonance studies. Atmos Environ 2008;42:1752–61. http://dx.doi.org/10.1016/j.etmosenv.2007.11.026.
[15] Hudson PK, Young MA, Kleiber PD, Grassian VH. Coupled infrared extinction spectra and size distribution measurements for several non-clay components of mineral dust aerosol (quartz, calcite, and dolomite). Atmos Environ 2008;42:5991–9.
[16] Hudson PK, Gibson ER, Young MA, Kleiber PD, Grassian VH. Coupled infrared extinction and size distribution measurements for several clay components of mineral dust aerosol. J Geophys Res 2008;113:D01201. http://dx.doi.org/10.1029/2007JD008791.
[17] Spitzer WG, Kleinman DA. Infrared lattice bands of quartz. Phys Rev 1961;121:1324–35. http://dx.doi.org/10.1103/PhysRev.121.1324.
[18] Wenrich ML, Chrsitensen PR. optical constants of minerals derived from emission spectroscopy: application to quartz. J Geophys Res 1996;101(B7):15921–31.
[19] Glotch TD, Rossman GR, Aharonson O. Mid-infrared (5–100 μm) reflectance spectra and optical constants of ten phyllosilicate minerals. Icarus 2007;192:605–22.
[20] Querry MR. Optical constants of minerals and other materials from the millimeter to the ultraviolet. Aberdeen, Md.: U.S. Army; 1987.
[21] Roush T, Pollack J, Orenberg J. Derivation of midinfrared (5–25 μm) optical constants of some silicates and palagonite. Icarus 1991;94:191–208.
[22] Lane MD. Midinfrared optical constants of calcite and their relationship to particle size effects in thermal emission spectra of granular calcite. J Geophys Res 1999;104(E6):14099–108.
[23] Long LL, Querry MR, Bell RJ, Alexander RW. Optical properties of calcite and gypsum in crystalline and powdered form in the infrared and far-infrared. Infrared Phys 1993;34:191–201.
[24] Lentz WJ. Generating Bessel functions in Mie scattering calculations using continued fractions. Appl Opt 1976;15(3):668–71.
[25] Deirmendijan D, Clasen R, Viezee W. Mie scattering with complex index of refraction. J Opt Soc Am 1961;51(6):620–33.

[26] Bohren CF, Huffman DR. Absorption and scattering of light by small particles. New York, USA: John Wiley & Sons; 1983.
[27] Legrand M, Dubovik O, Lapyonok T, Derimian Y. Accounting for particle non-sphericity in modeling of mineral dust radiative properties in the thermal infrared. J Quant Spectrosc Radiat Transf 2014;149:219–40. http://dx.doi.org/10.1016/j.jqsrt.2014.07.014.
[28] Min M, Hovenier JW, de Koter A. Shape effects in scattering and absorption by randomly oriented particles small compared to the wavelength. Astron Astrophys 2003;404:35–46.
[29] Chýlek P. Asymptotic limits of the Mie-scattering characteristics. J Opt Soc Am A 1975;65(11):1316–8.
[30] Acquista C, Cohen A, Cooney JA, Wimp J. Asymptotic behavior of the efficiencies in Mie scattering. J Opt Soc Am 1980;70(8):1023–5.
[31] Hulst vd. Light scattering by small particles. New York, U.S.A: Dover Publications, Inc.; 1980.
[32] Chýlek P, Klett JD. Absorption and scattering of electromagnetic radiation by prismatic columns: anomalous diffraction approximation. J Opt Soc Am A 1991;8(11):1713–20.
[33] Maslowska A, Flatau PJ, Stephens GL. On the validity of the anomalous diffraction theory to light scattering by cubes. Opt Commun 1994;107:35–40.
[34] Kemppinen O, Nousiainen T, Lindqvist H. The impact of surface roughness on scattering by realistically shaped wavelength-scale dust particles. J Quant Spectrosc Radiat Transf 2015;150:55–67. http://dx.doi.org/10.1016/j.jqsrt.2014.05.024.
[35] Klüser L, Kleiber PD, Holzer-Popp T, Grassian VH. Desert dust observation from space – Application of measured mineral component infrared extinction spectra. Atmos Environ 2012;54:419–27.
[36] Engelbrecht JP, McDonald EV, Gillies JA, Jayanty RKM, Casuccio G, Gertler AW. Characterizing mineral dust and other aerosols from the middle east – Part 1: ambient sampling. Inhal Toxicol 2009;21:297–326.
[37] Kleiber PD, Grassian VH, Young MA, Hudson PK. T-matrix studies of aerosol particle shape effects on IR resonance spectral line profiles and comparison with an experiment. J Geophys Res 2009;114:D21209. http://dx.doi.org/10.1029/2009JD012710.
[38] Carlon HR. Christiansen effect in IR spectra of soil-derived atmospheric dusts. Appl Opt 1979;18:3610–4.
[39] Chýlek P, Srivastava V, Pinnick RG, Wang RT. Scattering of electromagnetic waves by composite spherical particles: experiment and effective medium approximations. Appl Opt 1988;27:2396–404.
[40] Kandler K, Schütz L, Deutschner C, Ebert M, Hofmann H, Jäckel S, Jaenicke R, Knippertz P, Lieke K, Massling A, Petzold A, Schladitz A, Weinzierl B, Wiedensohler A, Zorn S, Weinbruch S. Size distribution, mass concentration, chemical and mineralogical composition and derived optical parameters of the boundary layer aerosol at Tinfou, Morocco, during SAMUM 2006. Tellus 2009;61B:32–50.
[41] Clarisse L, Coheur P-F, Prata F, Hadji-Lazaro J, Hurtmans D, Clerbaux C. A unified approach to infrared aerosol remote sensing and aerosol type specification. Atmos Chem Phys 2013;13:2195–221.
[42] Mishchenko MI, Travis LD, Mackowski DW. T-matrix computations of light scattering by nonspherical particles: a review. J Quant Spectrosc Radiat Transf 1996;55:535–75.
[43] Caquineau S, Gaudichet A, Gomes L, Legrand M. Mineralogy of Saharan dust transported over northwestern tropical Atlantic Ocean in relation to source regions. J Geophys Res 2002. http://dx.doi.org/10.1029/2001JD000247.
[44] Formenti P, Schütz L, Balkanski Y, Desboeufs K, Ebert M, Kandler K, Petzold A, Scheuvens D, Weinbruch S, Zhang D. Recent progress in understanding physical and chemical properties of African and Asian mineral dust. Atmos Chem Phys 2011;11:8231–56. http://dx.doi.org/10.5194/acp-11-8231-2011.